

When do feedforward microcircuits produce beyond-pairwise correlations?

Andrea K. Barreiro, Julijana Gjorgjieva,
Fred Rieke, and Eric Shea-Brown

September 7, 2022

Abstract

Describing the collective activity of neural populations is a daunting task: the number of possible patterns grows exponentially with the number of cells, resulting in practically unlimited complexity. Recent empirical studies, however, suggest a vast simplification in how multi-neuron spiking occurs. The activity patterns of some circuits produce patterns that are completely described by pairwise-correlated firing events; in other cases, both pairwise and higher-order correlations occur. What determines the difference? Here, we study the emergence of higher-order correlations in feedforward circuits with different architectures and inputs. We quantify this by comparing the responses of mechanistic circuit models vs. “null” descriptions in which all higher-than pairwise correlations have been removed, known as pairwise maximum entropy models. We find that responses to bimodal input signals shared by all circuit elements deviate substantially from purely pairwise predictions, while responses to unimodal inputs, regardless of connectivity, do not. A circuit model based on intracellular recordings from retinal ganglion cells further shows that a broad range of light signals induce unimodal inputs to spike generators, providing a simple explanation for the success of pairwise models in this system. These findings identify circuit-level mechanisms that produce higher-order spiking statistics in neural ensembles, and specific mechanisms that do not.

Introduction

Information in neural circuits is often encoded in the activity of large, highly interconnected neural populations. The combinatoric explosion of possible responses of such circuits poses major conceptual, experimental, and computational challenges. How much of this potential complexity is realized? What do statistical regularities in population responses tell us about circuit architecture? Can simple circuit models with limited interactions among cells capture the relevant information content? These questions are central to our understanding of neural coding and decoding.

Two developments have advanced studies of synchronous activity in recent years. First, new experimental techniques provide access to responses from the large groups of neurons necessary to adequately sample synchronous activity patterns [1]. Second, maximum entropy approaches from statistical physics have provided a powerful approach to distinguish true higher-order synchrony (correlations) from that explainable by pairwise correlations among neurons [2,3]. These approaches have produced diverse findings. In some instances, activity of neural populations is extremely well described by pairwise correlations alone, so that pairwise maximum entropy models provide a nearly complete description [4,5]. In other cases, while pairwise models bring major improvements over independent descriptions, they fail to fully capture the data [6–12]. The range of empirical findings highlights the need to understand the network features that control the statistical complexity of synchronous activity patterns.

Several themes have emerged from efforts to link the correlation structure of spiking activity to circuit mechanisms using generalized [13–16] and biologically-based models [9, 17, 18]. Two findings are particularly relevant for the present study. First, thresholding nonlinearities in circuits with Gaussian input signals can generate higher than second-order correlations [13]; these effects, however, cause at most modest deviations from predictions of pairwise maximum entropy models over a wide range of input parameters [15]. Second, perturbation approaches can explain why maximum entropy models with purely pairwise interactions capture circuit behavior when the population firing rate is low (i.e. the total number of firing events from all cells in the same small time window is small) [16]. The success of pairwise models in capturing multivariate spiking data, however, extends well beyond this low firing rate regime. The basis of this unexpected success of pairwise models remains unclear.

Here, we characterize the ability of pairwise maximum entropy (PME) models to capture the responses of feedforward circuits where correlations arise from common input sources (see Figure 1). We choose *feedforward* circuits, in particular, to gain insight into the success of pairwise models in classes of retinal ganglion cells [4,5] that are known to have small or negligible coupling [19]. We find that responses of neurons receiving broadly divergent common input are well described by PME models under a wide range of conditions. However, networks with bimodal inputs deviate substantially from PME fits, while networks with identical connectivity but unimodal inputs do not. Thus success of PME models does not bear a simple relation to network architecture. Networks based on measured properties of primate parasol ganglion cells generated responses closely approximated by PME models, providing insight into why the measured activity patterns in these cells are well captured by such models [4,5].

Results

A geometric approach to identifying higher-order correlations among triplets of cells

A commonly used strategy for identifying higher-order correlations is to compare multi-neuron spike data against a description in which any higher-order correlations have been removed in a principled way. Such a description may be given by a maximum entropy model [2, 3], as we now describe.

Maximum entropy methods provide a means to determine how much of the potential complexity of response patterns produced by large neural populations can be captured by a given set of constraints. The idea is to identify the most unstructured, or maximum entropy, distribution consistent with the constraints. Comparing the predicted and measured probabilities of different responses tests whether the constraints used are sufficient to explain the network activity, or whether additional constraints need to be considered. Such additional constraints would produce additional structure in the predicted response distribution, and hence lower the entropy.

A common approach is to limit the constraints to a given statistical order — for example, to consider only the first and second moments of the distributions, which are determined by the mean and pairwise correlations. In the context of spiking neurons, we denote μ_i as the firing rate of neuron i and ρ_{ij} as the (Pearson’s) correlation coefficient of the firing events of neurons i and j . The distribution with the largest entropy for a given μ_i and ρ_{ij} is often referred to as the *pairwise maximum entropy* (PME) model. The problem is made simpler if we consider only permutation-symmetric spiking patterns, in which the firing rate and correlation do not depend on the identity of the cells; i.e. $\mu_i = \mu$, $\rho_{ij} = \rho$ for $i \neq j$. Thus the PME problem is to identify the distribution that maximizes the response entropy given the constraints μ and ρ . This section provides a geometric, and hence visual, approach to this problem.

We consider a permutation-symmetric network of three cells with binary responses. We assume that the response is stationary and uncorrelated in time. From symmetry, the possible network responses are

$$\begin{aligned} p_0 &= P(0, 0, 0) \\ p_1 &= P(1, 0, 0) = P(0, 1, 0) = P(0, 0, 1) \\ p_2 &= P(1, 1, 0) = P(1, 0, 1) = P(0, 1, 1) \\ p_3 &= P(1, 1, 1), \end{aligned}$$

where p_i denotes the probability that a particular set of i cells spike and the remaining $3 - i$ do not. Possible values of (p_0, p_1, p_2, p_3) are constrained by the fact that P is a probability distribution, meaning that the sum of p_i over all eight states is one. We will rearrange these response probabilities to define a more convenient coordinate system below.

Possible solutions to the PME problem take the form of exponential functions character-

ized by two parameters, λ_1 and λ_2 , which serve as Lagrange multipliers for the constraints,

$$P(x_1, x_2, x_3) = \frac{1}{Z} \exp[\lambda_1(x_1 + x_2 + x_3) + \lambda_2(x_1x_2 + x_2x_3 + x_1x_3)]. \quad (1)$$

The factor Z normalizes P to be a probability distribution. We can combine the individual probabilities of events

$$\begin{aligned} p_0 &= \frac{1}{Z} \\ p_1 &= \frac{1}{Z} \exp(\lambda_1) \\ p_2 &= \frac{1}{Z} \exp(2\lambda_1 + \lambda_2) \\ p_3 &= \frac{1}{Z} \exp(3\lambda_1 + 3\lambda_2) \end{aligned}$$

to yield the equation

$$\frac{p_3}{p_0} = \left(\frac{p_2}{p_1} \right)^3. \quad (2)$$

This is equivalent to the condition that the *strain* measure defined in [20] be zero (in particular, the strain is negative whenever $p_3/p_0 - (p_2/p_1)^3 < 0$, a condition identified in [20] as corresponding to sparsity in the neural code). Equation 2 defines, implicitly, a two-dimensional surface in the three-dimensional space of possible probability distributions which we call the *maximum entropy surface*. The family of distributions consistent with a given μ and ρ forms a line (the *iso-moment line*) in this space [18]. The PME fit is the intersection of this line with the surface defined by Equation 2.

This geometrical description of the PME problem takes a particularly simple form in an alternative coordinate space:

$$\begin{aligned} f_p &= p_3 + p_0 \\ f_{1p} &= \frac{p_3}{p_3 + p_0} \\ f_{1m} &= \frac{p_2}{p_2 + p_1}. \end{aligned} \quad (3)$$

This set of coordinates separates events based on whether they are “pure” (all cells either spike, or do not) or “mixed” (only a subset of cells spike). f_p is the fraction of observed events that are pure; of these states, f_{1p} is the fraction of pure events with more cells spiking than not (p_3 vs. p_0). f_{1m} is the fraction of mixed states with more cells firing than not (p_2 vs. p_1). Possible probability distributions are contained within a cube in this coordinate space: $0 \leq f_p, f_{1p}, f_{1m} \leq 1$. The PME approximation is still given by the intersection of the iso-moment line for a given μ and ρ with the maximum entropy surface, as shown in Figure 2.

The convenience of this coordinate system is apparent when the maximum entropy constraint (Equation 2) is rewritten:

$$f_{1p} = \frac{f_{1m}^3}{1 - 3f_{1m} + 3f_{1m}^2}. \quad (4)$$

This surface is independent of f_p — i.e. the maximum entropy surface forms a curve when projected into the (f_{1p}, f_{1m}) -plane. In addition, each iso-moment line lies in a constant f_p plane (see Figure 2, center row). The distance of an observed distribution P from the surface is thus easily visualized; this distance, as we will show below, gives an indication of how close P comes to being a pairwise maximum entropy distribution.

We use the Kullback-Leibler divergence, $D_{KL}(P, \tilde{P})$, to quantify the accuracy of the PME approximation \tilde{P} to a distribution P . We can motivate this measurement on information theoretic grounds; $D_{KL}(P, \tilde{P})$ is approximately $-L$, where L is the averaged log ratio of the likelihood that data drawn from the distribution P was instead drawn from the model \tilde{P} [4, 21]. For example, if $D_{KL} = 1$, the average relative likelihood that a single sample from P — i.e. a single network response — in fact came from \tilde{P} is 2^{-1} .

To get an intuitive picture of $D_{KL}(P, \tilde{P})$ throughout the cube of possible distributions P , we view this quantity along constant- f_p slices in Figure 3. $D_{KL}(P, \tilde{P})$ increases with distance from the constraint curve (Equation 4); along the iso-moment line for a given (μ, ρ) , $D_{KL}(P, \tilde{P})$ is convex with a minimum of zero at $P = \tilde{P}$ (detailed calculations are given in Materials and Methods). Therefore, for any choice of μ and ρ , the observed distribution with the maximal deviation from its pairwise maximum entropy approximation will occur at one of the two points where the iso-moment line reaches the boundary of the cube. The *global* maximum of $D_{KL}(P, \tilde{P})$ will, therefore, also occur on the boundary.

To assess the numerical significance of $D_{KL}(P, \tilde{P})$, we can compare it with the maximal achievable value for any symmetric distribution on three spiking cells. For three cells, this value is 1 (or 1/3 bits per neuron), achieved by the XOR operation [22]. This distribution is illustrated in Figure 2. We will find that distributions produced by feedforward circuits fall far short of this value.

In summary, we have shown that identifying high-order correlations in the joint firing patterns of three cells is equivalent to showing that spiking probabilities lie a substantial distance from a constraint surface that is easy to visualize. Given this geometric description of the problem, we next consider how the distance from the constraint surface depends on circuit connectivity, nonlinear properties of the individual circuit elements, and the statistics of the input signals (Figure 1).

When do triplet inputs produce higher-order correlations in spike outputs?

We considered a simple feedforward circuit in which three spiking cells sum and threshold their inputs. Each cell j received an independent input I_j and a “triplet” — or global — input I_c that is shared among all three cells. Each cell compared the total input $S_j = I_c + I_j$ with a

threshold Θ , which determined whether or not the cell spikes in that time bin. The nonlinear threshold can produce substantial differences between input and output correlations [23–27]. A parameter c determined the fraction of the total input variance σ^2 originating from the global input.

Unimodal inputs fail to produce higher-order correlations in three cell feedforward circuits

We first considered “unimodal” inputs, which were chosen from a distribution with a single peak (or range of most likely values). Gaussian inputs provide a natural example. If I_c and each I_j are gaussian, then the joint distribution of $\mathbf{S} = (S_1, S_2, S_3)$ is multivariate normal, and therefore characterized entirely by its means and covariances. Because the PME fit to a continuous distribution is precisely the multivariate normal that is consistent with the first and second moments, every such input distribution on \mathbf{S} *exactly* coincides with its PME fit. However, even with Gaussian inputs, outputs (which are now in the binary state space $\{0, 1\}^3$) will deviate from the PME fit [13, 15]. As shown below, non-Gaussian unimodal inputs can produce outputs with larger deviations. Nonetheless, these deviations in all cases are modest, and PME models were quite accurate descriptions of circuits with a broad range of unimodal inputs.

We considered a circuit of three cells with inputs I_c and I_j that could be Gaussian, uniform, or skewed. For each type of input distribution, we probed the output distribution across a range of values for c , σ , and Θ that explored “all” possible activity patterns. In particular, we covered a full range of firing rates, not limited to the low firing rate regime treated in [16]. Figure 4A-C shows observed distributions for different marginal input statistics (left column). The central column compares all observed distributions with the PME constraint curve, projected into the (f_{1p}, f_{1m}) -plane.

The right column of Figure 4A-C shows $D_{KL}(P, \tilde{P})$ as a function of c and σ for the value of Θ that maximized $D_{KL}(P, \tilde{P})$ (or one of them, if multiple such values exist). Different scales are used to emphasize the structure of the data. For the unimodal cases shown, D_{KL} peaked in regions with comparatively low input variance ($\sigma < 1$) and large relative strength of common input ($c > 0.5$). However, $D_{KL}(P, \tilde{P})$ never reached a very high numerical value for unimodal inputs; the maximal values achieved for Gaussian, skewed, and uniform distributions are 0.00376, 0.0152, and 0.0186 respectively (compare with Figure 2). Thus hundreds or thousands of samples would be required to reliably distinguish the outputs of these networks from the PME approximation.

Clear patterns emerged when we viewed $D_{KL}(P, \tilde{P})$ as a function of *output* spiking statistics rather than *input* statistics. Figure 5A-C show the same data that is contained in the center column of Figure 4, but now plotted with respect to the output firing rate (recall that all three cells fire with the same rate). The data were segregated according to the correlation coefficient ρ between the responses of cell pairs, with lighter shades indicating increasing correlation. For a fixed correlation, there was generally a one-to-one relationship between firing rate and $D_{KL}(P, \tilde{P})$. For unimodal distributions (Figure 5A-B), $D_{KL}(P, \tilde{P})$ showed a double-peaked relationship with firing rate, with larger values attained at low and

high firing rates, and a minimum in between. Additionally, $D_{KL}(P, \tilde{P})$ had a non-monotonic relationship with spike correlation: it increased from zero for low values of correlation, obtained a maximum for an intermediate value, and then decreased. These limiting behaviors agree with intuition: a spike pattern that is completely uncorrelated can be described by an independent distribution (a special cases of PME model), and one that is perfectly correlated can be completely described via (perfect) pairwise correlations alone.

Bimodal triplet inputs can generate higher-order correlations in three cell feed-forward circuits

Having shown that a wide range of unimodal common inputs produced spike patterns that are well-approximated by PME fits, we next examined bimodal inputs. Figure 4D shows results from a simple ensemble of bimodal inputs — Bernoulli-distributed common and independent inputs — that produced moderate deviations from the pairwise approximation. The common input was “1” with probability p and “0” with probability $1 - p$. The independent inputs were each chosen to be “1” with probability q and “0” with probability $1 - q$. The threshold of the cells was between 1 and 2, so that spiking required *both* common and independent inputs to be active. The space of possible spiking distributions was explored by varying p and q .

This circuit produced response distributions that deviated moderately from PME fits, and these distributions preferentially lie on one side of the constraint curve (Figure 4D, center). The largest values of $D_{KL}(P, \tilde{P})$ occurred where moderate correlated input is coupled with strong background input ($q > 0.5$; Figure 4D, right), and reached values that are five times higher than was found for a unimodal distribution (the maximal value achieved is 0.091). The location of this maximum value is demonstrated in Figure 2.

Both of these observations can be explained by direct calculation of the spiking probabilities. Substituting the probabilities of different events — $p_0 = 1 - p + p(1 - q)^3$, $p_1 = pq(1 - q)^2$, $p_2 = pq^2(1 - q)$ and $p_3 = pq^3$ — into the PME constraint equation (Equation 2) and dividing by q^3 , we can write

$$\frac{p}{1 - p + p(1 - q)^3} = \frac{1}{(1 - q)^3} \quad (5)$$

which gives us an intuition for how to violate the constraint; for a fixed q , we manipulate the left-hand side by changing p .

Another way to view this is by making the observation that the right hand side of Equation 2 can be written without reference to the probability of common input; because $P[1 \text{ spike} | I_c = 0] = 0$ and $P[2 \text{ spikes} | I_c = 0] = 0$, one may write

$$\begin{aligned} \frac{p_2}{p_1} &= \frac{P[2 \text{ spikes} | I_c = 1]P[I_c = 1]}{P[1 \text{ spike} | I_c = 1]P[I_c = 1]} \\ &= \frac{P[2 \text{ spikes} | I_c = 1]}{P[1 \text{ spike} | I_c = 1]} \end{aligned} \quad (6)$$

which has no dependence on the statistics of the common input. So the *left* hand side of the constraint equation can be manipulated by shifting p , without making any changes to the right hand side.

In Figure 5C, we again present values of $D_{KL}(P, \tilde{P})$ as a function of the firing rate and pairwise correlation elicited by the full range of possible bimodal inputs. We see that $D_{KL}(P, \tilde{P})$ is maximized at a single, intermediate firing rate, and for correlation values near 0.6.

An analytical explanation for unimodal vs. bimodal effects

Further support for the difference between unimodal and bimodal inputs comes from analytical calculations of $D_{KL}(P, \tilde{P})$ for small deviations from the PME constraint surface of Equation 2. We summarize the results of this calculation here; details are in Materials and Methods. We considered narrow distributions of common input I_c , with a small parameter \sqrt{c} characterizing the distribution width (equivalently, the common input had a variance of c). By approximating the distribution of network outputs by a Taylor series, we found that $D_{KL}(P, \tilde{P})$ depended on c^3 for unimodal distributions — i.e the low order terms in c dropped out (for *symmetric* distributions, such as Gaussian, the growth was even smaller: c^4). For bimodal distributions, on the other hand, $D_{KL}(P, \tilde{P})$ grew like c^2 . The key point is that, as the strength of common input signals increased, circuits with bimodal inputs diverged from the PME fit much more rapidly than those with unimodal inputs.

When do pairwise inputs produce higher-order correlations in spike outputs?

In the previous section, we considered permutation-symmetric distributions generated by a single, global, common input. Another class of permutation-symmetric distributions can be generated when common inputs are shared *pairwise* — i.e. by two cells but not three at once. We now show that significant departures from the pairwise maximum entropy model (PME) can be generated with pairwise bimodal inputs. This provides a specific example in which network architecture and output statistics are not in simple correspondence.

Our circuit setup included three cells, each of which received and summed two inputs and spiked if this sum exceeded a threshold. We denote the inputs I_{12} , I_{23} , I_{13} so that cell 2 received I_{12} and I_{23} , and so forth. Each input was chosen from a binary distribution with parameters m and r so that $P[I_{ij} = m] = r$ and $P[I_{ij} = 0] = 1 - r$. Without loss of generality, we chose $m = 1$ and chose the threshold such that $1 < \Theta < 2$. Therefore, both pairwise inputs to a cell must be active in order for a cell to fire. It is not possible in this circuit for precisely *two* cells to fire; for two cells to fire (say cell 1 and cell 2), both inputs to each cell must be active. However, this implies that both inputs to cell 3 (I_{13} and I_{23}) are active as well. If two cells fire, then the third must fire as well; that is, $p_2 = 0$.

The remaining probabilities are easily computed by itemizing and computing the probabilities for each event and are as follows: $p_3 = r^3$, $p_1 = r^2(1-r)$, and $p_0 = 3r(1-r)^2 + (1-r)^3$. This distribution has a unique PME fit consistent with both the first and second moments.

However, the PME fit can be far from the actual distribution; we found that $D_{KL}(P, \tilde{P})$ depended on the input rate r and could exceed 0.5. Thus observation of the network response (single draw from P) would, on average, have a likelihood ratio of 0.7 of coming from \tilde{P} versus P , and observation of 15 network responses would have a likelihood ratio of less than 0.01.

Scaling of higher-order correlations with population size

The permutation-symmetric architectures we have considered can be scaled up to more than three cells in several natural ways; for example, we can consider N cells with a global common input. The pairwise input structure can also be scaled up to consider N cells on a ring, with each pair of adjacent cells receiving a common, pairwise input (see Figure 1). We next used the methods described in the previous section to study networks with these architectures and sizes up to $N = 16$.

We first considered a sequence of models in which a set of N threshold spiking units received global input I_c (with mean 0 and variance $\sigma^2 c$) and an independent input I_j (with mean 0 and variance $\sigma^2(1 - c)$). The output of each cell was determined by summing and thresholding these inputs. The probability distribution of network outputs was computed as described in the Methods and then fit with a pairwise maximum entropy distribution. As for the three cell networks above, we explored a range of σ , c , and Θ and recorded the maximum value of $D_{KL}(P, \tilde{P})$ between the observed distribution P and its PME fit \tilde{P} . Figure 6 shows this D_{KL}/N (i.e. entropy per cell [15]) for Gaussian, uniform, skewed, and bimodal input distributions.

We found that the maximum $D_{KL}(P, \tilde{P})$ increased roughly linearly with N for bimodal inputs, and superlinearly for unimodal inputs. The relative ordering found at $N = 3$ — that the maximal achievable $D_{KL}(P, \tilde{P})$ is lowest for Gaussian inputs, followed by skewed, uniform, and bimodal inputs consecutively — remained the same. The sidebar of Figure 6 shows that the probability distributions produced by these inputs qualitatively agree with this trend: departures from PME were more pronounced for global bimodal inputs (top histogram) than for global unimodal inputs (third histogram from top). Overall, we note that for any of the global inputs, it becomes easier to statistically distinguish between spiking distributions and their PME fits as N increases. For example, at $N = 16$, the value $D_{KL}/N \approx 0.1$ for bimodal global inputs corresponds to a likelihood ratio of 0.33 that a single draw from P (single network output) in fact came from the PME fit \tilde{P} versus P ; a likelihood < 0.01 is reached for 4 draws.

We next considered pairwise inputs for $N > 3$ cells by adopting a ring structure with nearest-neighbor common inputs (illustrated in Figure 1). For unimodal inputs, we computed $D_{KL}(P, \tilde{P})$ while varying σ and Θ ; for bimodal inputs, we varied the probability r of each Bernoulli input. Figure 6 shows the maximal $D_{KL}(P, \tilde{P})$ per neuron. Circuits with bimodal pairwise inputs showed appreciable values that are still about half of that reported for bimodal global inputs. The relatively large deviation at $N = 3$ receded, replaced by deviations that were similar to those seen for global, unimodal inputs. For pairwise unimodal inputs, values of $D_{KL}(P, \tilde{P})$ remained very small.

To summarize, the impact of input statistics on maximal $D_{KL}(P, \tilde{P})$ persists from $N = 3$ up to $N = 16$. Other parameters being equal, bimodal inputs can generate a larger $D_{KL}(P, \tilde{P})$ than unimodal inputs. For a particular choice of input marginals, global inputs can generate greater deviations than purely pairwise inputs (with the exception of one case, $N = 3$). However, the goodness of the PME fit alone does not distinguish between global and pairwise anatomical projections. With these principles in hand, we then studied a more biologically realistic network model.

An experimentally constrained model for correlated firing in retinal ganglion cells

PME approaches have been effective in capturing the activity of retinal ganglion cell (RGC) populations [4–6]. This success does not have an obvious anatomical correlate — i.e. there are multiple opportunities in the retinal circuitry for interactions among three or more ganglion cells. Why do these apparently fail to generate higher-order correlations? To answer this question, we explored the properties of circuits composed of cells with input statistics and spike-generating mechanisms fit directly to intracellular recordings.

RGC model

We modeled a single RGC in two stages. We give an overview here; details are provided in Materials and Methods. First, we characterized the light-dependent excitatory and inhibitory synaptic inputs to cell k ($g_k^{\text{exc}}(t), g_k^{\text{inh}}(t)$) in response to randomly fluctuating light inputs $s(t)$ via a linear-nonlinear model, e.g.:

$$g_k^{\text{exc}}(t) = N^{\text{exc}}[L^{\text{exc}} * s_k(t) + \eta_k^{\text{exc}}], \quad (7)$$

where N^{exc} is a static nonlinearity, L^{exc} is a linear filter, and η_k^{exc} is an effective input noise that captures variability in the response to repetitions of the same time-varying stimulus.

Second, we used Equation 7 and an equivalent expression for $g_k^{\text{inh}}(t)$ as inputs to an integrate-and-fire model incorporating a nonlinear voltage and history dependent term to account for refractory interactions between spikes [28]. We fit the parameters of this model to a dynamic clamp experiment [29,30] in which currents corresponding to $g^{\text{exc}}(t)$ and $g^{\text{inh}}(t)$ (with appropriate driving forces) were injected into a cell and the resulting voltage response measured.

The prescription above provided a flexible model that we used to study the response of an RGC to a wide range of light inputs. Specifically, we simulated RGC models with light stimuli that were (1) constant, (2) time-varying and spatially uniform, and (3) varying in both space and time. Correlations between cell inputs arose from shared stimuli and from shared noise originating in the retinal circuitry [19]. In each case, we determined whether the accuracy of a PME fit to the outputs was predictable based on the input distributions and our prior results. We focused on excitatory conductances because they appear to play a larger role in shaping spike timing [19]. To compare our results with empirical studies, constant light and spatially, temporally fluctuating checkerboard stimuli were used as in [4,5].

Constant light

To simulate constant light conditions, we set $s_k(t) = 0$ for $k = 1, 2, 3$, so that the cells received only Gaussian correlated noises η_k^{exc} and η_k^{inh} and constant excitatory and inhibitory conductances. The magnitude, correlation timescale, and pairwise correlations of η_k^{exc} and η_k^{inh} were chosen as described in Materials and Methods, based on experimentally measured values in [19]. Time-dependent conductances were generated and used as inputs to a simulation of three model RGCs. To test for sufficiency of simulation length, we report the standard deviation in event probabilities from a total of 20 simulations (see Materials and Methods). Under these conditions the excitatory conductances were unimodal and broadly Gaussian. As expected from earlier results on threshold models, the spiking distributions were well-modeled by a PME fit, as shown in Figure 7A; $D_{KL}(P, \tilde{P})$ is 0.0004. This agrees with the very good fits found experimentally in [4] under constant light stimulation.

Full-field stimulus

For full-field simulations, each cell received the same stimulus, $s_k(t) = s(t)$, where $s(t)$ refreshes every few milliseconds with an independently chosen value from some marginal distribution. The shared stimulus produced strong pairwise correlation between excitatory conductances of neighboring cells. However, from results on our threshold model, we expect that this is not the determining factor in whether or not spiking outputs will be well-modeled by a PME fit; rather, the shape of the marginal distribution of inputs (here, excitatory conductances) should be more important than the strength of pairwise correlations.

We first examined the effects of different marginal statistics of light stimuli, standard deviation of full-field flicker, and refresh rate on the marginal distributions of excitatory conductances. For a short refresh rate (8 ms) and small flicker variance (1/6 or 1/3 of baseline light intensity), temporal averaging via the filter L^{exc} and the approximately linear form of N^{exc} over these light intensities produced a unimodal, approximately Gaussian distribution of excitatory conductances, regardless of whether the flicker is drawn from a Gaussian or binary distribution (see Figure 7B-C, center panels). For a slower refresh rate (100 ms) and large flicker variance (1/2 or 3/4 of baseline light intensity), excitatory conductances had multi-modal and skewed features, again regardless of whether the flicker is drawn from a gaussian or binary distribution (Figure 7D). Other parameters being equal, binary light input produced more skewed conductances. While some conductance distributions had multiple local maxima, these were never well-separated, with the envelope of the distribution still resembling a skewed distribution.

Overall, high-pass filtering — a consequence of the differentiating linear filter in Equation 17 and illustrated in Figure 7D — significantly reduced the bimodality of the input stimuli (compare Figure 7D left (input, blue histogram) vs. center (output, conductance histogram)). We verified that filters without the biphasic, high-pass shape of Equation 17 (i.e., without the negative dip at longer time lags) produced conductance distributions that more completely reflect the bimodal shape of binary light inputs (data not shown). This raises the intriguing suggestion that greater $D_{KL}(P, \tilde{P})$ could occur for other cell types pri-

marily characterized via monophasic filters, or for light stimuli that lead to distinct operating ranges in which such filters dominate.

As expected from our studies with the simple thresholding model of spike generation, the largely unimodal shape of input distributions was reflected in the ability of PME fits to accurately capture spiking distributions. The distances from PME fits $D_{KL}(P, \tilde{P})$ computed from the observed distributions were small, never exceeding 0.0061; these are numbers comparable to what is achievable by a skewed input into a thresholding unit. To test the sensitivity of this conclusion to uncertainty in the observed probability distribution, we performed an analysis in which the data was divided into 20 subsets and the maximum entropy analysis was performed individually on each subset. The resulting KL-distance remained small, never exceeding 0.011. In summary, even high-contrast, bimodal, highly spatially correlated stimulus variations do not produce a large departure from the PME fit.

When we examined all of the spiking distributions produced in this sequence of simulations, we found a common pattern in the way in which the PME fit deviated from observed distributions. Single spiking events were over-predicted by PME fits, whereas double spiking events were under-predicted. We note that this is the same situation observed in our simple threshold model with bimodal global inputs (see Figure 3 and Materials and Methods), and corresponds to the case of negative strain identified by Ohiorhenuan et al. [20]. This finding is extremely robust; upon perturbing the distributions by estimated standard errors, as described in Materials and Methods, only 17 out of 480 perturbed distributions showed a positive strain.

Spatially varying stimulus

Finally, moving beyond full field light stimuli, we asked whether pairwise maximum entropy models will capture RGC responses to stimuli with varying spatial scales. We fixed stimulus dynamics to match the two cases that yielded the highest $D_{KL}(P, \tilde{P})$ under the full field protocol: for Gaussian stimuli, a 40 ms refresh rate and $\sigma = 1/3$, and for binary stimuli, a 8 ms refresh rate and $\sigma = 1/2$. The stimulus was generated as a random checkerboard with squares of variable size; each square in the checkerboard, or *stixel*, was drawn independently from the appropriate marginal distribution and updated at the corresponding refresh rate. The conductance input to each RGC was then given by convolving the light stimulus with its receptive field, where the stimulus is positioned with a fixed rotation and translation relative to the receptive fields. This position was drawn randomly at the beginning of each simulation and held constant throughout. See Figure 8D,G for examples, and Materials and Methods for further details.

The RGC spike patterns remained very well described by PME models for the full range of spatial scales. Figure 8A shows this by plotting $D_{KL}(P, \tilde{P})$ vs. stixel size. Values of $D_{KL}(P, \tilde{P})$ increased with spatial scale, sharply rising beyond $128 \mu\text{m}$, where a stixel is approximately the same size as a receptive field center. The points at $512 \mu\text{m}$ are from the corresponding full field simulations, illustrating that introducing spatial scale via stixels produces even closer fits by PME models.

Values reported in Figure 8A are *averages* of $D_{KL}(P, \tilde{P})$ produced by 5 random stimulus

positions. At stixel sizes of $128\ \mu\text{m}$ and $256\ \mu\text{m}$, the resulting spiking distributions differed significantly from position to position: see Figure 8B for an example at $256\ \mu\text{m}$. This variability does not occur for smaller spatial scales; see Figure 8C for an example at $60\ \mu\text{m}$. Moreover, for $128\ \mu\text{m}$ and $256\ \mu\text{m}$ stixel sizes, certain stimulus positions produced significant cell-to-cell heterogeneity across the 3 RGCs, in both the excitatory conductances (one example is shown in Figure 8E) and in spike patterns (Figure 8F). This did not occur at smaller scales (e.g., Figure 8H-I). We emphasize that PME models gave excellent fits to data regardless of heterogeneity in RGC responses, as illustrated in Figure 8F; over all 20 subsimulations (as above), and over all individual stixel positions, we found a maximal $D_{KL}(P, \tilde{P})$ value of 0.0194.

Discussion

We use simple mechanistic models to identify when feedforward neural circuits produce spike patterns with higher-order correlations, and when they do not. We accomplish this by comparing circuit outputs with pairwise maximum entropy (PME) descriptions, in which all higher-order correlations have been removed in a principled way, leaving only pairwise interactions. Overall, the magnitude of higher-order correlations that occur for our simple feedforward step cover a range which is much lower than the maximum theoretically attainable values for a general spiking pattern in the same size network. Several simple principles emerge that determine how close a given network is to its PME fit. First, bimodal input distributions produced stronger higher-order correlations than unimodal distributions. Second, networks with shared inputs among all cells produced greater higher-order correlations than those with pairwise inputs (except for the case of three cell networks receiving bimodal input). Our overall finding held for networks with nonlinear integrate-and-fire units based on measured properties of retinal ganglion cells, thus providing an explanation for why population activity of ganglion cells is well captured by PME models.

Comparison with empirical studies

How do our maximum entropy fits compare with empirical studies? In terms of $D_{KL}(P, \tilde{P})$ — equivalently, the average log-likelihood ratio that observed data drawn from P is drawn from the model \tilde{P} versus the true distribution P — numbers obtained from our RGC models are very similar to those obtained by experiments on retinal ganglion cells [4, 5]. We find that $D_{KL}(P, \tilde{P}) = 0.0004$ under constant light conditions, compared to an experimental value of 0.0008 [4] (inferred from a reported likelihood ratio of 0.99944). Under full-field, time varying light conditions, as well as spatiotemporally varying stixel simulations, we find average log-likelihood ratios of up to one order of magnitude larger – bounded above by 0.007. We can view this as a model of the checkerboard experiments of [4], for which close fits by PME distribution were also observed (likelihood numbers were not reported).

An alternative measure used in the literature comes from normalizing $D_{KL}(P, \tilde{P})$ by the corresponding distance of the distribution from an *independent maximum entropy* fit $D_{KL}(P, P_1)$, where P_1 is the highest entropy distribution consistent with the mean firing rates of the cells (in other words, the independent model P_1 is given by the product of single-cell marginal firing probabilities). Shlens et al. [4, 5] and Schneidman et al. [6] use

$$\begin{aligned}\Delta &= \frac{D_{ind} - D_{pair}}{D_{ind}} \\ &= 1 - \frac{D_{KL}(P, \tilde{P})}{D_{KL}(P, P_1)}\end{aligned}\tag{8}$$

using their notation $D_{ind} \equiv D_{KL}(P, P_1)$ and $D_{pair} \equiv D_{KL}(P, \tilde{P})$. A value of $\Delta = 1$ (100%) indicates that the pairwise model perfectly captures the additional information left out of the independent model. When we probe our RGC circuit in settings that are comparable to

experimental settings, we find that the values of Δ that are produced by our RGC model are close to those found by [4, 6]. We obtain $\Delta = 97.2\%$ under constant illumination, which is near the range reported by [4] (97.8 – 99.2%). For full-field stimuli we find a range of numbers from 96.1 – 99.6%.

The simple threshold models that we have developed, meanwhile, give us a roadmap for how circuits could be driven in such a way as to lower Δ . Figure 5D-F show Δ plotted as a function of firing rate for the data presented in Figure 5A-C: circuits of $N = 3$ cells receiving global common inputs. We observe that $\Delta \approx 1$ for gaussian and skewed inputs over a broad range of firing rates and pairwise correlation coefficients, but that values of Δ can be depressed by 10-15% in the presence of a bimodal common input. Indeed, Shlens et al. [4] showed that adding global bimodal inputs to a purely pairwise model can lead to a comparable departure in Δ . Our results are consistent with this finding, and explicitly demonstrate that the bimodality of the inputs is the determining characteristic that leads to this departure.

While meaningful in an experimental study with non-negligible pairwise correlations, we caution that using Δ as a metric can be problematic when an idealized circuit is explored over its full range of parameters, because it may flag “uninteresting” cases in which cells are nearly independent, and a pairwise model adds little additional value. Specifically, if D_{ind} is small (the true distribution is well-approximated by P_1), then Δ may be appreciably far from 1 although D_{pair} is small. Thus, a poor pairwise maximum entropy fit, as measured by Δ (that is, $\Delta < 1$) is not necessarily indicative of a poor performance in $D_{KL}(P, \tilde{P})$. For example, in the bimodal common input case (Figure 5F), the very lowest values of Δ are achieved for low correlation ρ ; in essence, when the independent model already does a good job of representing the output distribution. As suspected this performance is not reflected in Figure 5C, where low correlation gives low $D_{KL}(P, \tilde{P})$. In summary, Δ can be as low as 0.5 for distributions that are barely perceptibly different when measured by the Kullback-Leibler divergence.

Figure 5G-H extends our observations to a circuit of $N = 12$ cells forced by Gaussian and skew inputs respectively. Here, we find that small Δ is primarily a result of extremely low firing rates, where P is nearly independent (dominated by 0 spiking events, which means the distribution is well-modeled by independent non-spiking neurons) and the improvement of the pairwise model over the independent model is negligible. This is also the regime where $1 - \Delta$, as proven by [16], is linear in $N - 2$. If a nontrivial deviation of Δ (from 1) is observed for $N\nu < 1$ (in this case, $N = 3$), then $1 - \Delta$ must continue to grow; equivalently, Δ must decrease. The growth of $1 - \Delta$ with N for particular points in this region is illustrated in Figure 5I.

Using correlation structure to infer anatomical structure

We address two questions about the relationship between the architecture of feedforward circuits and the statistical structure of the spike patterns that they produce, based on our comparisons between global-input and pairwise nearest-neighbor network architectures in the Results.

First, if a circuit produces spike patterns that deviate substantially from pairwise maximum-entropy (PME) predictions, can we conclude that it has beyond-pairwise anatomical projections — that is, common inputs received by more than two cells? We have shown that there is no single answer, without knowing more about how a circuit is constructed.

For small group of $N = 3$ cells, the answer is no: we find that, among all cases we study, the largest deviation from PME predictions occurs for *purely pairwise* (binary) inputs, so that departures from PME models do not imply departures from pairwise nearest-neighbor network architectures. For larger N , the answer is a qualified yes: for marginal statistics of a given type, we show in Figure 6 that the greatest deviations from PME models do correspond to global common (as opposed to purely pairwise) inputs. However, without knowing input marginals, values of D_{KL} are still not predictive of anatomy: for example, if $N = 16$, then roughly the same values of $D_{KL}(P, \tilde{P})$ follow from global inputs with uniform marginals as for pairwise nearest-neighbor inputs with binary marginals.

Second, if a circuit produces spike patterns that are well-described by PME models, does this imply that it has a pairwise architecture? By the same reasoning as above, the answer depends on N and marginal statistics. For $N > 3$ and knowledge of input marginals, better fits by PME imply pairwise nearest-neighbor connectivity; otherwise, such inferences cannot be made.

Scope and open questions

Our first set of findings are for a set of circuit models with a simple thresholding nonlinearity at each cell. These models were chosen to be simple enough to allow analytical insights and a complete numerical study. While a more realistic retinal ganglion cell model demonstrates that these findings, based on a simple threshold model, do carry over to describe the spiking statistics of a more realistic spiking model (here, a time-dependent, nonlinear integrate-and-fire system), there are many aspects of circuits left unexplored by our studies of feedforward circuits.

Most prominent is heterogeneity. Our studies apply to cells with identical response properties and thus are not directly comparable to studies such as [6] which examine correlation structures among multiple cell types. For larger networks, feedforward connections with variable spatial profiles occur, between the extremes of “nearest neighbor” and global input connections. It is also possible that more complex input statistics could lead to greater higher-order correlations [31]. Finally, Figure 6 indicates that some trends in $D_{KL}(P, \tilde{P})$ vs. N appear to become nonlinear for $N \gtrsim 10$; for larger networks, our qualitative findings could change.

A plethora of other network features could also lead to higher-order correlations, including multilayer feedforward structures, together with lateral and feedback coupling. Preliminary results, not shown here, indicate that simple, biophysically motivated feedback mechanisms in our three-cell thresholding circuit can generate a 20-fold increase in $D_{KL}(P, \tilde{P})$; this may be a mechanism for developing the higher-order correlations found in cortex [7, 10, 11, 32]. Another outstanding question is the impact of higher-order correlations (or the lack thereof) on the level of encoded information and the encoding spike patterns (i.e., their sparsity, [20]).

We hope that the present study, as one of the first that connects circuit mechanisms to higher-order correlations, will contribute to future research along these lines.

Materials and Methods

D_{KL} and distance from PME surface

To see that $D_{KL}(P, \tilde{P})$ is convex along an iso-moment line, we consider $D_{KL}(P, \tilde{P})$ as P varies so as to remain on an iso-moment line. Letting \tilde{f}_{1m} and \tilde{f}_{1p} be the coordinates of the PME fit, and defining $dm = f_{1m} - \tilde{f}_{1m}$ and $dp = f_{1p} - \tilde{f}_{1p}$, we find

$$dp = \frac{(f_p - 1)/3}{\sqrt{f_p^2 + (1 - f_p)^2/9}} dx$$

$$dm = \frac{f_p}{\sqrt{f_p^2 + (1 - f_p)^2/9}} dx$$

where dx is an increment of distance along the iso-moment line. Inverting Equations 3 and substituting the results into the definition of D_{KL} , we can write

$$\begin{aligned} D_{KL}(P, \tilde{P}) &= f_p(1 - \tilde{f}_{1p}) \left(1 - \frac{dp}{1 - \tilde{f}_{1p}}\right) \log \left(1 - \frac{dp}{1 - \tilde{f}_{1p}}\right) \\ &+ (1 - f_p)(1 - \tilde{f}_{1m}) \left(1 - \frac{dm}{1 - \tilde{f}_{1m}}\right) \log \left(1 - \frac{dm}{1 - \tilde{f}_{1m}}\right) \\ &+ (1 - f_p)\tilde{f}_{1m} \left(1 + \frac{dm}{\tilde{f}_{1m}}\right) \log \left(1 + \frac{dm}{\tilde{f}_{1m}}\right) \\ &+ f_p\tilde{f}_{1p} \left(1 + \frac{dp}{\tilde{f}_{1p}}\right) \log \left(1 + \frac{dp}{\tilde{f}_{1p}}\right). \end{aligned} \quad (9)$$

This is a convex function of dx ; we can see this by observing that each of the four terms is a function of the form

$$F(dx) = \alpha \left(1 + \frac{dx}{\beta}\right) \log \left(1 + \frac{dx}{\beta}\right)$$

(in the first term, for example, we have $\alpha = f_p(1 - \tilde{f}_{1p})$ and $\beta = -(1 - \tilde{f}_{1p})$). This can be readily shown to be convex by taking the second derivative with respect to dx and verifying that it is positive:

$$F''(dx) = \frac{\alpha}{\beta^2 \left(1 + \frac{dx}{\beta}\right)},$$

where we can verify that $\alpha > 0$ and $|dx| < \beta$. The sum of convex functions is likewise convex. Because $D_{KL}(P, Q)$ is non-negative for any distributions P and Q , $D_{KL}(P, \tilde{P})$ achieves its unique minimum along an iso-moment line at $P = \tilde{P}$, and it must monotonically increase as a function of $|dx|$.

To get an intuitive picture of $D_{KL}(P, \tilde{P})$ as it varies in the (f_p, f_{1p}, f_{1m}) -coordinate space, we view this quantity along constant- f_p slices (Figure 3). $D_{KL}(P, \tilde{P})$ increases with distance from the constraint curve. Generally, the range of this distance peaks at $f_p = 0.25$.

To further quantify the relationship between distance and D_{KL} , we approximate the logarithms in Equation 9 for small arguments and find that D_{KL} increases quadratically with distance for small arguments:

$$D_{KL}(P, \tilde{P}) \approx (dx)^2 C(f_p, \tilde{f}_{1m}) + O(dx^3) \quad (10)$$

where

$$\begin{aligned} C(f_p, \tilde{f}_{1m}) &= \frac{f_p(1-f_p)^2/9}{f_p^2 + (1-f_p)^2/9} \frac{(1-3\tilde{f}_{1m} + 3\tilde{f}_{1m}^2)^2}{\tilde{f}_{1m}^3(1-\tilde{f}_{1m})^3} \\ &+ \frac{f_p^2(1-f_p)}{f_p^2 + (1-f_p)^2/9} \frac{1}{\tilde{f}_{1m}(1-\tilde{f}_{1m})} \end{aligned}$$

Numerical sampling of 3 cell network

For general circuit set-ups, it may be necessary to probe the output distribution by sampling. In the case of global input, however, it is more computationally efficient and accurate to compute the output spiking probability distribution using quadrature. To be concrete, a set of $N = 3$ threshold spiking units is forced by a common input I_c (drawn from a probability distribution $P_C(y)$) and an independent input I_j (drawn from a probability distribution $P_I(y)$). The output of each cell x_j is determined by summing and thresholding these inputs:

$$x_j = H(I_j + I_c - \Theta)$$

Conditioned on I_c , the probability of each spike is given by:

$$\begin{aligned} \mathbf{Prob}[x_j = 1 \mid I_c = a] &= \mathbf{Prob}[I_j + a - \Theta > 0] \\ &= \mathbf{Prob}[I_j > \Theta - a] \\ &= \int_{\Theta - a}^{\infty} P_I(y) dy \end{aligned}$$

Similarly, we have the conditioned probability that $x_j = 0$:

$$\begin{aligned} \mathbf{Prob}[x_j = 0 \mid I_c = a] &= \mathbf{Prob}[I_j + a - \Theta < 0] \\ &= \mathbf{Prob}[I_j < \Theta - a] \\ &= \int_{-\infty}^{\Theta - a} P_I(y) dy \end{aligned}$$

Because these are conditionally independent, the probability of any spiking event $(x_1, x_2, x_3) = (A_1, A_2, A_3)$ is given by the integral of the product of the conditioned probabilities against the density of the common input.

$$\mathbf{Prob}[x_1 = A_1, x_2 = A_2, x_3 = A_3] = \int_{-\infty}^{\infty} dy P_C(y) \prod_{j=1}^3 \mathbf{Prob}[x_j = A_j \mid I_c = y] \quad (11)$$

The integrand in the previous equation is numerically evaluated via an adaptive quadrature routine, such as Matlab's `quad`. This is easily generalized to an arbitrary number of cells N .

Unimodal inputs I_j, I_c were chosen from different marginals with mean 0 and variance σ^2 . For Gaussian input, $P(x) \propto e^{-x^2/2\sigma^2}$; for uniform inputs, $P(x) \propto 1$ for $|x| < \sqrt{3\sigma^2}$ and 0 otherwise. For skewed input, $P(x) \propto (x - \mu)e^{-(x-\mu)^2/2a}$, for $x > -\mu$, where the parameter a sets the variance $(1 - \frac{\pi}{4})^2 a^2$ and shifting by $\mu = \sqrt{\frac{a\pi}{2}}$ ensures that the mean of $P(x)$ is zero

Bimodal triplet inputs always generate distributions with negative strain

Another information theoretic quantity that relates to the ability of a distribution to be characterized by a pairwise model is the strain:

$$\gamma = \frac{1}{8} \log \left(\frac{P(1, 1, 1)P(1, 0, 0)P(0, 1, 0)P(0, 0, 1)}{P(0, 0, 0)P(1, 1, 0)P(1, 0, 1)P(0, 1, 1)} \right).$$

Indeed, this quantity must be zero for any distribution that satisfies the PME constraint (Equation 2). Negative values of strain occur to the *left* side of the PME constraint curve in the (f_{1p}, f_{1m}) -plane, whereas positive values occur to the *right*.

For a circuit forced by common binary inputs, the simplicity of our setup allows us to show why observed distributions occur to the left side of the PME constraint curve. We approach this by showing that given the f_{1m} coordinate of an observed distribution, the f_{1p} coordinate is less than the PME fit would predict. A point on the constraint surface corresponding to a particular value of f_{1m} may be written

$$\begin{aligned} \tilde{f}_{1p} &= \frac{f_{1m}^3}{1 - 3f_{1m} + 3f_{1m}^2} \\ &= \frac{q^3}{q^3 + (1 - q)^3} \end{aligned}$$

whereas

$$f_{1p} = \frac{pq^3}{pq^3 + (1 - p) + p(1 - q)^3}$$

and

$$\begin{aligned} \frac{1}{f_{1p}} &= \frac{1 - p + p(q^3 + (1 - q)^3)}{pq^3} \\ &= \frac{1 - p}{pq^3} + \frac{1}{\tilde{f}_{1p}} \end{aligned}$$

This makes it clear that $\frac{1}{f_{1p}} \geq \frac{1}{\tilde{f}_{1p}}$ with equality if and only if $p = 1$. Therefore

$$f_{1p} < \tilde{f}_{1p} \tag{12}$$

unless $p = 1$, in which case they coincide.

According to Equation 12, p_0 is *under-predicted* by the PME model, whereas p_3 is *over-predicted*; this is precisely the condition of ‘‘sparse coding’’ [20].

An analytical explanation for unimodal vs. bimodal effects

We consider an analytical argument to support our numerical results that bimodal inputs generate larger deviations from PME model fits than unimodal inputs. As a metric, we consider $D_{KL}(P, \tilde{P})$ — where P and \tilde{P} are again the true and model distributions respectively — when we perturb an independent spiking distribution by adding a common, global input of variance \mathbf{c} . To simplify notation, the small parameter in the calculation will be denoted $\epsilon = \sqrt{\mathbf{c}}$.

We proceed by writing the KL-distance as a difference of entropies:

$$D_{KL}(P, \tilde{P}) = S(\tilde{P}) - S(P)$$

where the entropy of a probability distribution P is given

$$S(P) = -p_0 \log(p_0) - 3p_1 \log(p_1) - 3p_2 \log(p_2) - p_3 \log(p_3) \quad (13)$$

if we use the fact that the distributions are permutation-symmetric (i.e. $p_1 \equiv P(1, 0, 0) = P(0, 1, 0) = P(0, 0, 1)$). For each term $S(P)$ and $S(\tilde{P})$, we will derive a series expansion for each set of event probabilities.

We can compute the true distribution P using the expressions derived in Equation 11; to recap, let the common input have probability density $p(c)$, and the independent input to each cell have density $p_s(x)$. Let θ be the threshold for generating a spike (i.e., a “1” response). For each cell, a spike is generated if $x + c > \theta$, i.e., with probability

$$d(c) = \int_{\theta-c}^{\infty} p_s(x) dx .$$

Given c , this is conditionally independent for each cell. We can therefore write our probabilities by integrating over c as follows:

$$\begin{aligned} p_0 &= \int_{-\infty}^{\infty} p(c)(1 - d(c))^3 dc \\ p_1 &= \int_{-\infty}^{\infty} p(c)d(c)(1 - d(c))^2 dc \\ p_2 &= \int_{-\infty}^{\infty} p(c)d(c)^2(1 - d(c)) dc \\ p_3 &= \int_{-\infty}^{\infty} p(c)d(c)^3 dc \end{aligned} \quad (14)$$

We develop a perturbation argument in the limit of very weak common input. That is, $p(c)$ is close to a delta function centered at $c = 0$. Take $p(c)$ to be a scaled function

$$p(c) = \frac{1}{\epsilon} f\left(\frac{c}{\epsilon}\right) \quad (15)$$

We place no constraints on $f(c)$, other than that it must be normalized ($\mathbf{E}[1] = 1$) and that its moments must be finite (so $\mathbf{E}[c]$, $\mathbf{E}[c^2]$, and so forth must exist, where $\mathbf{E}[g(c)] \equiv \int_{-\infty}^{\infty} g(c)f(c)dc$).

For the moment, assume that the function $f(c)$ has a single maximum at $c = 0$. To evaluate the integrals above, we Taylor-expand $d(c)$ around $c = 0$. Anticipating a sixth-order term to survive, we keep all terms up to this order. This gives, for small y ,

$$d(y) \approx d(0) + \sum_{k=1}^6 a_k y^k + O(y^7)$$

where $a_1 = p_s(\theta)$ (the other coefficients a_2 - a_6 can be given similarly in terms of the independent input distribution at θ). Substituting this into the expressions for p_0 , etc., above, with $p(c)$ given as in Equation 15, gives us each event as a series in ϵ ; for example,

$$p_3 = d_0^3 + (3a_1 d_0^2 \mathbf{E}[c]) \epsilon + ((3a_1^2 d_0 + 3a_2 d_0^2) \mathbf{E}[c^2]) \epsilon^2 + \dots$$

The entropy $S(P)$ is now given by using these series expansions in Equation 13.

We note that our derivation does not rely on the fact that the distribution of common input is peaked at $c = 0$ in particular. For example, we could have a common input centered around μ . The common input distribution function would be of the form

$$p(c) = \frac{1}{\epsilon} f\left(\frac{c - \mu}{\epsilon}\right)$$

Changing ϵ regulates the variance, but doesn't change the mean or the peak (assuming, without loss of generality, that the peak of f occurs at zero). The peak of $p(c)$ now occurs at μ , and the appropriate Taylor expansion of $d(y)$ is

$$d(y) \approx d(\mu) + \sum_{k=1}^6 b_k (y - \mu)^k + O(y^7),$$

where the coefficients b_k now depend on the local behavior of d around μ . The expectations that appear in the expansion of p_3 , and so forth, are now centered moments taken around μ ; the calculations are otherwise identical. In other words, perturbation expansion requires the *variance* of the common input to be small, but not the mean.

For bimodal inputs, we consider a common input with a probability distribution of the following form:

$$p(c) = (1 - \epsilon^2) \frac{1}{\epsilon} f\left(\frac{x}{\epsilon}\right) + \epsilon^2 \frac{1}{\epsilon} f\left(\frac{x - 1}{\epsilon}\right)$$

so that most of the probability distribution is peaked at zero, but there is a second peak of higher order (here taken at $c = 1$, without loss of generality). Again, we approximate the

integrals given in Equations 14, and therefore the entropy $S(P)$, by Taylor expanding d ;

$$\begin{aligned} d(c) &\approx d(0) + \sum_{k=1}^6 a_k c^k + O(c^7); \quad (c \approx 0) \\ &\approx d(1) + \sum_{k=1}^6 b_k (c-1)^k + O((c-1)^7); \quad (c \approx 1) \end{aligned}$$

around the two peaks 0 and 1 respectively. For each integral we have the same contributions from the unimodal case, multiplied by $(1 - \epsilon^2)$, as well as the corresponding contributions from the second peak multiplied by ϵ^2 (these weightings are chosen so that the common input has variance of order ϵ^2 , as in the unimodal case). This makes clear at what order every term enters.

We now construct an expansion for the PME model \tilde{P} :

$$\tilde{P}(x_1, x_2, x_3) = \frac{1}{Z} \exp(\lambda_1(x_1 + x_2 + x_3) + \lambda_2(x_1 x_2 + x_2 x_3 + x_1 x_3))$$

We approach this problem by describing λ_1 and λ_2 as a series in ϵ . We match coefficients by forcing the first and second moments of \tilde{P} to match those of P — as they must. Specifically, take

$$\begin{aligned} \lambda_1 &= \tilde{\lambda} + \sum_{k=1}^6 \epsilon^k u_k + O(\epsilon^7) \\ \lambda_2 &= \sum_{k=1}^6 \epsilon^k v_k + O(\epsilon^7) \end{aligned}$$

where $\lambda_1 = \tilde{\lambda}$, $\lambda_2 = 0$ are the corresponding parameters from the independent case. The events $\tilde{p}_0, \tilde{p}_1, \tilde{p}_2$ and \tilde{p}_3 can be written as a series in ϵ . We then require that the mean and centered second moments of \tilde{P} match those of P ; that is

$$\begin{aligned} p_1 + 2p_2 + p_3 &= \tilde{p}_1 + 2\tilde{p}_2 + \tilde{p}_3 \\ p_2 + p_3 - (p_1 + 2p_2 + p_3)^2 &= \tilde{p}_2 + \tilde{p}_3 - (\tilde{p}_1 + 2\tilde{p}_2 + \tilde{p}_3)^2. \end{aligned}$$

At each order k , this yields a system of two linear equations in u_k and v_k ; we solve, inductively, up to the desired order; we now have \tilde{P} , and therefore $S(\tilde{P})$, as a series in ϵ .

Finally, we combine the two series to find that in the *unimodal* case,

$$\begin{aligned} D_{KL}(P, \tilde{P}) &= S(\tilde{P}) - S(P) \\ &= \epsilon^6 \left[\frac{a_1^6 (2 \mathbf{E}[c]^3 - 3 \mathbf{E}[c] \mathbf{E}[c^2] + \mathbf{E}[c^3])^2}{2(1-d_0)^3 d_0^3} \right] + O(\epsilon^7) \end{aligned} \quad (16)$$

If the first two odd moments of the distribution are zero (something we can expect for “symmetric” distributions, such as a Gaussian), then this sixth-order term is zero as well.

For the *bimodal* case

$$\begin{aligned} D_{KL}(P, \tilde{P}) &= S(\tilde{P}) - S(P) \\ &= \epsilon^4 \left[\frac{(d_1 - d_0)^6}{2(1 - d_0)^3 d_0^3} \right] + O(\epsilon^5) \end{aligned}$$

This last term depends on the distance $d_1 - d_0$, in other words, how much more likely the independent input is to push the cell over threshold when common input is “ON”. We can also view this as depending on the ratio $\frac{d_1 - d_0}{1 - d_0}$, which gives the fraction of previously non-spiking cells that now spike as a result of the common input.

The main point here, of course, is that $D_{KL}(P, \tilde{P})$ is of order ϵ^4 rather than ϵ^6 . So, as the strength of a common binary vs. unimodal input increases, spiking distributions depart from the PME more rapidly.

Experimentally-based model of a RGC circuit

We model the response of a individual RGC using data collected from a representative primate ON parasol cell. Similar response properties were observed in recordings from 16 other cells. To measure the relationship between light stimuli and synaptic conductances, the retina was exposed to a full-field, white noise stimulus. The cell was voltage clamped at the excitatory (or inhibitory) reversal potential $V_E = 0$ mV ($V_I = -60$ mV), and the inhibitory (or excitatory) currents were measured in response to the stimulus. These currents were then turned into equivalent conductances by dividing by the driving force of ± 60 mV; in other words

$$\begin{aligned} I^{\text{exc}} &= g^{\text{exc}}(V - V_E); & V - V_E &= -60 \text{ mV} \\ I^{\text{inh}} &= g^{\text{inh}}(V - V_I); & V - V_I &= 60 \text{ mV} \end{aligned}$$

The time-dependent conductances g^{exc} and g^{inh} were now injected into the same cell using a dynamic clamp (i.e., input current was instantaneously varied to maintain the correct relationship between the conductance and the instantaneous membrane voltage) and the voltage was measured at a resolution of 0.1 ms.

To model the relationship between the light stimulus and synaptic conductances into RGC, the current measurements I^{exc} and I^{inh} were fit to a linear-nonlinear model:

$$\begin{aligned} I^{\text{exc}}(t) &= N^{\text{exc}}[L^{\text{exc}} * s(t) + \eta^{\text{exc}}], \\ I^{\text{inh}}(t) &= N^{\text{inh}}[L^{\text{inh}} * s(t) + \eta^{\text{inh}}] \end{aligned}$$

where s is the stimulus, L^{exc} (L^{inh}) is a linear filter, N^{exc} (N^{inh}) is a nonlinear function, and η^{exc} (η^{inh}) is a noise term. The linear filter was fit by the function

$$L^{\text{exc}}(t) = P_{\text{exc}}(t/\tau_{\text{exc}})^{n_{\text{exc}}} \exp(-t/\tau_{\text{exc}}) \sin(2\pi t/T_{\text{exc}})$$

and the nonlinear filter by the polynomial

$$N^{\text{exc}} = A_{\text{exc}}x^2 + B_{\text{exc}}x + C_{\text{exc}};$$

L^{inh} and N^{inh} were fit using the same parametrization. The noise terms η_k^{exc} , η_k^{inh} were fit to reproduce the statistical characteristics of the residuals from this fitting. We simulated the noise terms η^{exc} and η^{inh} using Ornstein-Uhlenbeck processes with the appropriate parameters; these were entirely characterized by the mean, standard deviation, and time constant of autocorrelation $\tau_{\eta,\text{exc}}$ ($\tau_{\eta,\text{inh}}$), as well as pairwise correlation coefficients for noise terms entering neighboring cells. The noise correlation coefficients were estimated from the dual recordings of [19].

Linear filter parameters computed were $P_{\text{exc}} = -8 \times 10^4$ pA/s, $n_{\text{exc}} = 3.6$, $\tau_{\text{exc}} = 12$ ms, $T_{\text{exc}} = 105$ ms, and $P_{\text{inh}} = -1.8 \times 10^5$ pA/s, $n_{\text{inh}} = 3.0$, $\tau_{\text{inh}} = 16$ ms, $T_{\text{exc}} = 120$ ms. Nonlinearity parameters were $A_{\text{exc}} = -5 \times 10^{-5}$, $B_{\text{exc}} = 0.42$, $C_{\text{exc}} = -57$, and $A_{\text{inh}} = 1 \times 10^4$, $B_{\text{inh}} = 0.37$, $C_{\text{inh}} = 250$. Noise parameters were measured to be $\text{mean}(\eta_k^{\text{exc}}) = 30$, $\text{std}(\eta_k^{\text{exc}}) = 500$, $\tau_{\eta,\text{exc}} = 22$ ms, and $\text{mean}(\eta_k^{\text{inh}}) = -1200$, $\text{std}(\eta_k^{\text{inh}}) = 780$, $\tau_{\eta,\text{inh}} = 33$ ms. In addition, excitatory (inhibitory) noise to different cells η_k^{exc} , η_j^{exc} (η_k^{inh} , η_j^{inh}) had a correlation coefficient of 0.3 (0.15).

Model fitting

We create a model of the cell as a nonlinear integrate-and-fire model using the method of Badel et al. [28], in which the membrane voltage is assumed to respond as

$$\frac{dV}{dt} = F(V, t - t_{\text{last}}) + \frac{I_{\text{input}}(t)}{C} \quad (17)$$

where C is the cell capacitance, t_{last} is the time of the last spike before time t , and $I_{\text{input}}(t)$ is a time-dependent input current. We use the current-clamp data, which yields cell voltage in response to the input current $I_{\text{input}}(t) = g^{\text{exc}}(t)(V - V_E) + g^{\text{inh}}(t)(V - V_I)$, to fit a function $F(V, t)$. When voltage data is segregated according to the (binned) time since the last spike, the $I - V$ curve is well fit by a function of the form

$$F(V) = \frac{1}{\tau_m} (E_L - V + \Delta_T e^{(V - V_T)/\Delta_T}) \quad (18)$$

The membrane time constant τ_m , resting potential (E_L), spike width Δ_T and knee of the exponential curve V_T are parameterized as a function of $t - t_{\text{last}}$. Our model neuron comprises Equations (17, 18) for $V < V_{\text{threshold}}$, with a voltage reset $V_{\text{reset}} = -65$ mV when V reaches $V_{\text{threshold}} = -54$ mV.

The capacitance was inferred from the voltage trace data by finding, at a voltage value where the voltage/membrane current relationship is approximately Ohmic, the value of C that minimizes error in the relation Equation 17 [28]. The estimated value was $C = 28$ pF.

Cell receptive field

We defined each cell's stimulus as the linear convolution of an image with its receptive field. The receptive fields include an "on" center and an "off" surround, as in [33]:

$$s_j(\vec{x}) = \exp\left(-\frac{1}{2}(\vec{x} - \vec{x}_j)\mathbf{Q}(\vec{x} - \vec{x}_j)\right) - k \exp\left(-\frac{1}{2}r(\vec{x} - \vec{x}_j)\mathbf{Q}r(\vec{x} - \vec{x}_j)\right)$$

where the parameters k and $1/r$ give the relative strength and size of the surround. \mathbf{Q} specifies the shape of the center and was chosen to have a 1 standard deviation (SD) radius of $50\ \mu\text{m}$ and to be perfectly spherical. The receptive field locations \vec{x}_1 , \vec{x}_2 , and \vec{x}_3 were chosen so that the 1 SD outlines of the receptive field centers will tile the plane (i.e. they just touch). Other parameters used were $k = 0.3$, $r = 0.675$.

Convergence testing

To test the sensitivity of our results to sampling, we ran 20 simulations of length 10^5 ms under each condition. These were used to estimate standard errors in both the probability distribution over spiking events and $D_{KL}(P, \tilde{P})$. For example, in the constant light case, we generated the following distribution on spiking events: $P(0, 0, 0) = 0.658 \pm 0.002$, $P(0, 0, 1) = 0.0924 \pm 0.0005$; $P(0, 1, 0) = 0.0919 \pm 0.0007$, $P(1, 0, 0) = 0.0910 \pm 0.0007$, $P(0, 1, 1) = 0.0200 \pm 0.0003$, $P(1, 0, 1) = 0.0202 \pm 0.0003$, $P(1, 1, 0) = 0.0201 \pm 0.0003$, and $P(1, 1, 1) = 0.0059 \pm 0.0001$. Numbers reported in the Results are, unless specified otherwise, produced by collating the data from the 20 simulations.

To test our finding that the observed distributions were well-modeled by the PME fit, we also performed the PME analysis on each of the 20 simulations for each stimulus condition. While in general $D_{KL}(P, \tilde{P})$ can be quite sensitive to perturbations in P , the numbers remained small under this analysis. To confirm that our results for $D_{KL}(P, \tilde{P})$ are sufficiently resolved to remove bias from sampling, we performed an analysis in which we collect the 20 simulations in subgroups of 1, 2, 4, 5, 10, and 20, and plot the mean D_{KL} with estimated standard errors. As expected (e.g. [34]), bias decreases as the length of subgroup increases and asymptotes at — or before — the full simulation length. Results are shown in Figure S1 for the RGC simulations under full-field stimulation, as well as two representative cases with “stixel” stimuli. An example result is also shown for the simple thresholding model, for which sampling was also used in the pairwise inputs cases shown in Figure 6.

Finally, to test the robustness of our finding that the strain $\gamma < 0$ for the full-field RGC simulations, we perturbed our spiking event distributions randomly, with perturbations weighted by the estimated standard errors. This was repeated 20 times for each stimulus condition. Out of the resulting 480 perturbations (20 each for 24 stimulus conditions), $\gamma > 0$ in only 17 trials.

Financial Disclosure

This research was supported by NSF grant DMS-0817649 and by a Career Award at the Scientific Interface from the Burroughs-Wellcome Fund (ESB), by the Howard Hughes Medical Institute and by NIH grant EY-11850 (FMR), and a Cambridge Overseas Research Studentship (JG). The funders had no role in study design, data collection and analysis, decision to publish, or preparation of the manuscript.

References

- [1] Baudry M, Taketani M, editors (2006) *Advances in Network Electrophysiology Using Multi-Electrode Arrays*. New York: Springer Press.
- [2] Jaynes ET (1957) Information theory and statistical mechanics. *Physiol Rev* 106: 620-630.
- [3] Jaynes ET (1957) Information theory and statistical mechanics II. *Physiol Rev* 108: 171-190.
- [4] Shlens J, Field GD, Gauthier JL, Grivich MI, Petrusca D, et al. (2006) The structure of multi-neuron firing patterns in primate retina. *Journal of Neuroscience* 26: 8254–8266.
- [5] Shlens J, Field GD, Gauthier JL, Greschner M, Sher A, et al. (2009) The structure of large-scale synchronized firing in primate retina. *Journal of Neuroscience* 29: 5022–5031.
- [6] Schneidman E, Berry (II) MJ, Segev R, Bialek W (2006) Weak pairwise correlations imply strongly correlated network states in a neural population. *Nature* 440: 1007–1012.
- [7] Tang A, Jackson D, Hobbs J, Smith JL, Patel H, et al. (2008) A maximum entropy model applied to spatial and temporal correlations from cortical networks *in vitro*. *Journal of Neuroscience* 28: 505–518.
- [8] Yu S, Huang D, Singer W, Nikolic D (2008) A small world of neuronal synchrony. *Cerebral Cortex* 18: 2891–2901.
- [9] Martignon L, Deco G, Laskey K, Diamond M, Freiwald W, et al. (2000) Neural coding: higher-order temporal patterns in the neurostatistics of cell assemblies. *Neural Comp* 12: 2621–53.
- [10] Montani F, Ince RAA, Senatore R, Arabzadeh E, Diamond ME, et al. (2009) The impact of high-order interactions on the rate of synchronous discharge and information transmission in somatosensory cortex. *Philosophical Transactions of the Royal Society A* 367: 3297–3310.
- [11] Ohiorhenuan IE, Mechler F, Purpura KP, Schmid AM, Hu Q, et al. (2010) Sparse coding and high-order correlations in fine-scale cortical networks. *Nature* 466: 617–21.
- [12] Santos GS, Gireesh ED, Plenz D, Nakahara H (2010) Hierarchical interaction structure of neural activities in cortical slice cultures. *The Journal of Neuroscience* 30: 8720–8733.
- [13] Amari S, Nakahara H, Wu S, Sakai Y (2003) Synchronous firing and higher-order interactions in neuron pool. *Neural Computation* 15: 127–142.

- [14] Krumin M, Shoham S (2009) Generation of spike trains with controlled auto- and cross-correlation functions. *Neural Comp* 21: 1642–64.
- [15] Macke JH, Berens P, Ecker AS, Tolias AS, Bethge M (2009) Generating spike trains with specified correlation coefficients. *Neural Computation* 21: 397–423.
- [16] Roudi Y, Nirenberg S, Latham PE (2009) Pairwise maximum entropy models for studying large biological systems: When they can work and when they cant. *PLoS Computational Biology* 5: e1000380.
- [17] Roudi Y, Tyrcha J, Hertz J (2009) Ising model for neural data: Model quality and approximate methods for extracting functional connectivity. *Physical Review E* 79: 051915.
- [18] Bohte SM, Spekreijse H, Roelfsema PR (2000) The effects of pair-wise and higher-order correlations on the firing rate of a postsynaptic neuron. *Neural Computation* 12: 153–179.
- [19] Trong PK, Rieke F (2008) Origin of correlated activity between parasol retinal ganglion cells. *Nature Neuroscience* 11: 1343–1351.
- [20] Ohiorhenuan IE, Victor JD (2010) Information-geometric measure of 3-neuron firing patterns characterizes scale-dependence in cortical networks. *Journal of Computational Neuroscience* : 10.1007/s10827-010-0257-0.
- [21] Cover TM, Thomas JA (1991) *Elements of information theory*. New York: Wiley.
- [22] Schneidman E, Still S, Berry (II) MJ, Bialek W (2003) Network information and connected correlations. *Physical Review Letters* 91: 238701.
- [23] de la Rocha J, Doiron B, Shea-Brown E, Josic K, Reyes A (2007) Correlation between neural spike trains increases with firing rate. *Nature* 448: 802–806.
- [24] Vilela RD, Lindner B (2009) Comparative study of different integrate-and-fire neurons: Spontaneous activity, dynamical response, and stimulus-induced correlation. *Physical Review E* 80: 031909.
- [25] Shea-Brown E, Josić K, Doiron B, de la Rocha J (2008) Correlation and synchrony transfer in integrate-and-fire neurons: Basic properties and consequences for coding. *Phys Rev Lett* 100: 108102.
- [26] Marella S, Ermentrout GB (2008) Class-II neurons display a higher degree of stochastic synchronization than class-I neurons. *Physical Review E* 77: 041908.
- [27] Barreiro AK, Shea-Brown ET, Thilo EL (2010) Timescales of spike-train correlation for neural oscillators with common drive. *Physical Review E* 81: 011916.

- [28] Badel L, Lefort S, Brette R, Petersen CCH, Gerstner W, et al. (2007) Dynamic I-V curves are reliable predictors of naturalistic pyramidal-neuron voltage traces. *Journal of Neurophysiology* 99: 656–666.
- [29] Sharpe LT, Whittle P, Nordby K (1993) Spatial integration and sensitivity changes in the human rod visual system. *J Physiol* 461: 235-246.
- [30] Murphy GJ, Rieke F (2006) Network variability limits stimulus-evoked spike timing precision in retinal ganglion cells. *Neuron* 52: 511-524.
- [31] Bethge M, Berens P (2008) Near-maximum entropy models for binary neural representations of natural images. In: *Advances in Neural Information Processing Systems* 20. pp. 97–104.
- [32] Oizumi M, Ishii T, Ishibashi K, Okada M (2010) Mismatched decoding in the brain. *Journal of Neuroscience* 30: 4815–4826.
- [33] Chichilnisky EJ, Kalmar RS (2002) Functional asymmetries in ON and OFF ganglion cells of primate retina. *Journal of Neuroscience* 22: 2737–2747.
- [34] Paninski L (2003) Estimation of entropy and mutual information. *Neural Computation* 15: 1191–1253.

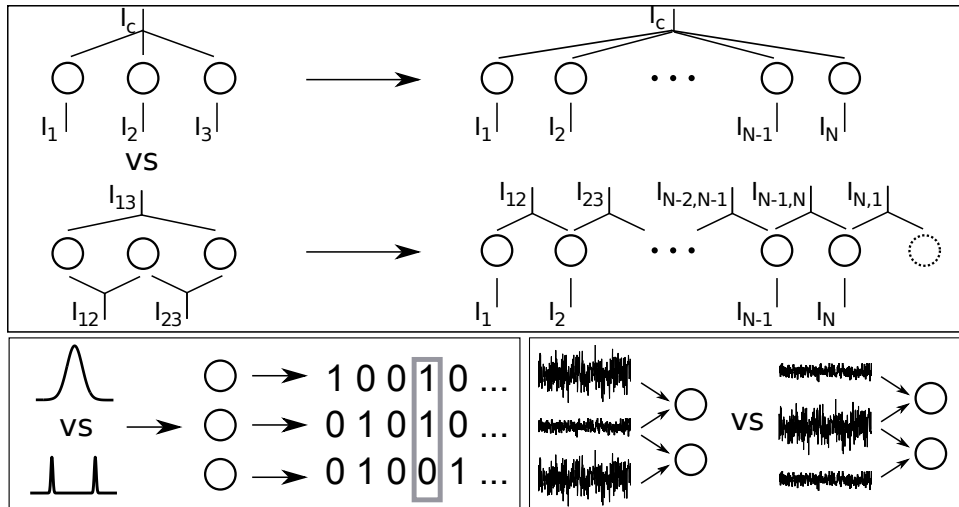


Figure 1: Schematic showing different axes on which we explore feedforward circuits in this study. (Top) Network architecture: global vs. pairwise inputs and scaling up system size N . (Bottom left) Input statistics: unimodal vs. bimodal marginal statistics. (Bottom right) Varying strength of common input.

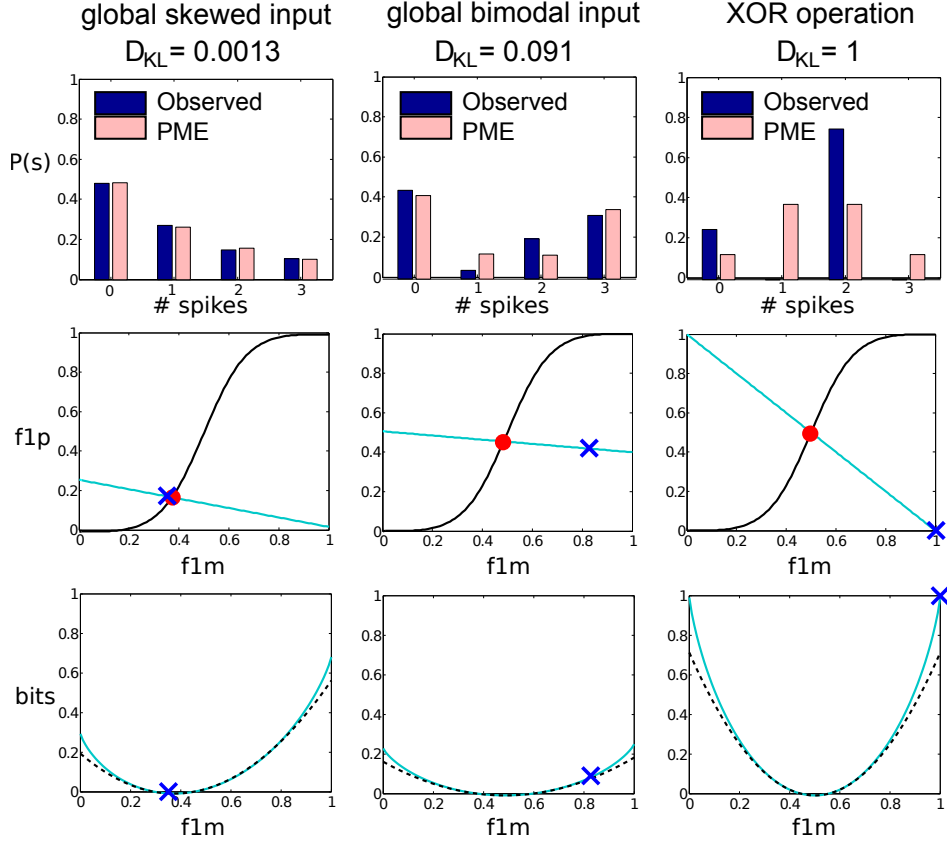


Figure 2: Examples of spiking distributions with small, intermediate, and large deviations from PME models. (Top row) Bar plot contrasting three distributions with their pairwise maximum entropy (PME) fits. The probability shown is the total probability of all events with a certain number of spikes. From left: global skewed input, global binary input, XOR operator. $D_{KL}(P, \tilde{P})$, is from left, 0.0013 (skewed), 0.091 (bimodal), and 1 (XOR). (Middle row) The same distributions (crosses) projected into the (f_{1m}, f_{1p}) -plane and their corresponding PME fits (circles). The cyan line is the *iso-moment line* of all distributions with the same first and second moments, and the black curve is the PME constraint surface. (Bottom row) $D_{KL}(P, \tilde{P})$ along the iso-moment line (cyan solid) and the approximation in Equation 10 (black dashed).

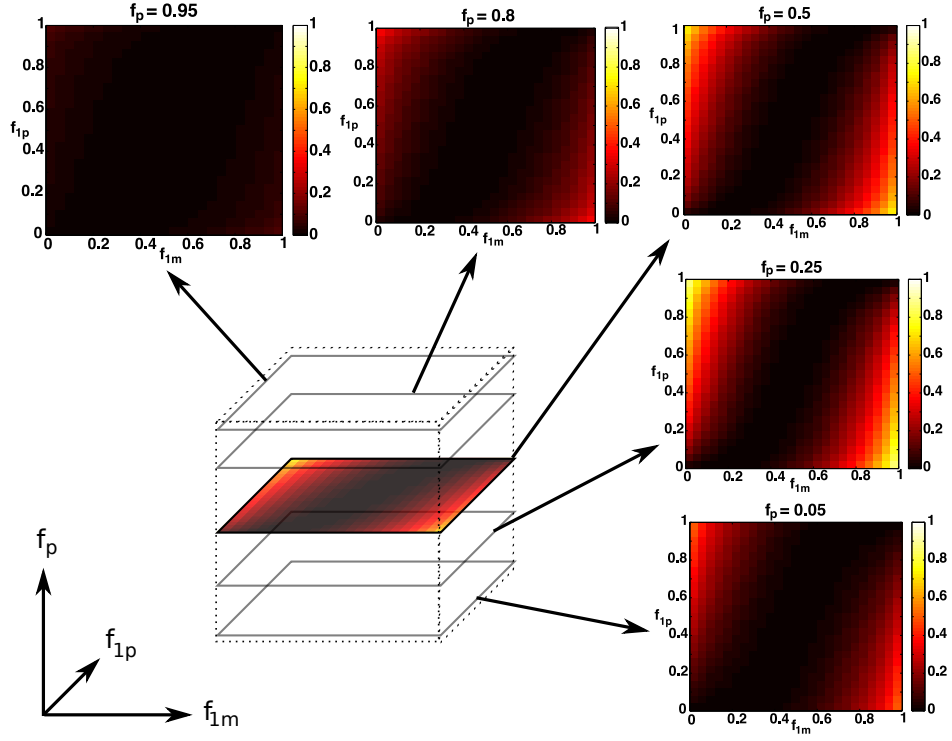


Figure 3: Geometrical organization of $D_{KL}(P, \tilde{P})$ within the space of three-cell spiking distributions. Outer plots: Slices of $D_{KL}(P, \tilde{P})$ along surfaces $f_p = \text{constant}$. Center: schematic of the (f_p, f_{1p}, f_{1m}) coordinate space. Counterclockwise from lower right: $f_p = 0.05, 0.25, 0.5, 0.8, 0.95$. $f_p = 0.25$ contains the maximal attainable $D_{KL}(P, \tilde{P})$ over all admissible P . $f_p = 0.616$ contains the maximal attainable D_{KL} from pairwise bimodal inputs (see Results).

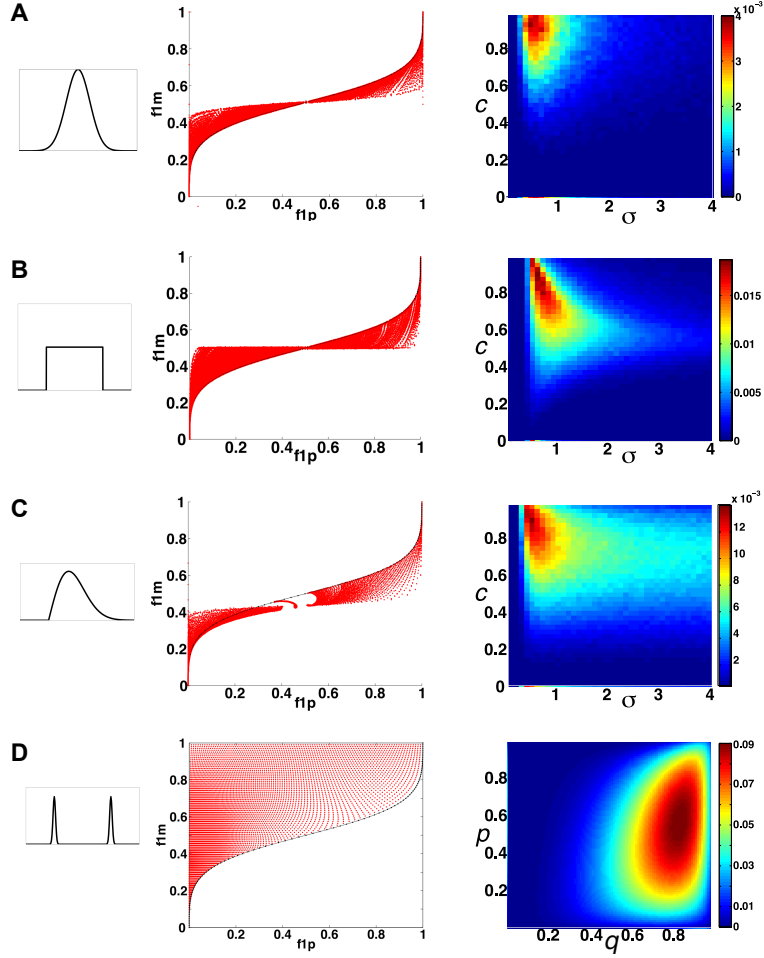


Figure 4: Deviation from PME fit for circuits receiving independent and (global) common input. Results shown for $N = 3$; (A) Gaussian, (B) uniform, (C) skewed, and (D) bimodal. For each choice of marginal input statistics, possible input parameters are varied over a broad range as described in the Results; over $c \in [0, 1]$, $\sigma \in [0, 4]$, and $\Theta \in [-1, 3]$ (unimodal inputs), over $p \in [0, 1]$ and $q \in [0, 1]$ (bimodal inputs). (Left column) Schematic of input distributions. (Center column) Projection of all distributions onto the (f_{1p}, f_{1m}) -plane. (Right column) For the value of Θ for which the maximal value is achieved, a slice of $D_{KL}(P, \tilde{P})$ (unimodal inputs); contour plot of $D_{KL}(P, \tilde{P})$ where $1 < \Theta < 2$ (bimodal inputs).

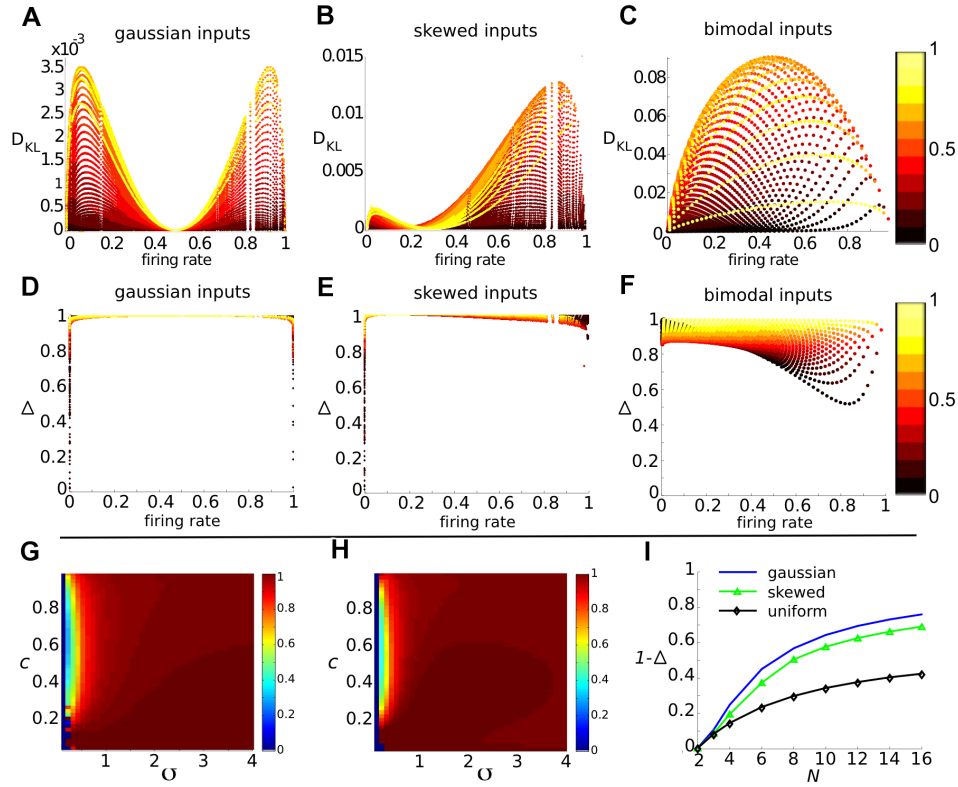


Figure 5: Relationship between measures of higher-order correlations and other output firing statistics. (A-C) $D_{KL}(P, \tilde{P})$ versus firing rate $\mathbf{E}[x_1]$, for all data obtained on $N = 3$ spiking cells. In each panel, data is organized by ρ , from dark ($\rho \in (0, 0.1)$) to light ($\rho \in (0.9, 1)$); (A) Gaussian, (B) skewed, (C) bimodal. (D-F) Δ (defined in Discussion) versus firing rate $\mathbf{E}[x_1]$, for all data obtained on $N = 3$ spiking cells. Data is organized by correlation coefficient ρ , as in panels (A-C); D) Gaussian, E) skewed, F) bimodal. (G-H) Δ for (G) Gaussian and (H) skewed input, for $N = 12$. (I) $1 - \Delta$ vs. N for Gaussian, skewed and uniform inputs at a fixed value of c and σ ($c = 0.56$; for Gaussian and skewed, $\sigma = 0.2$; for uniform, $\sigma = 0.6$)

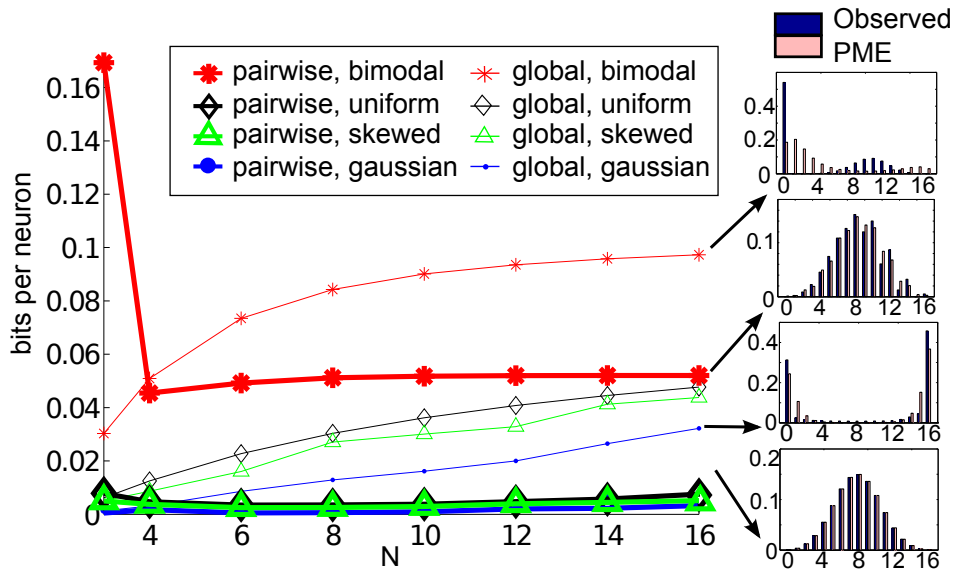


Figure 6: Maximal deviation from PME fit for circuit forced by either global or local input against background noise as N increases. For each N , possible input parameters are ranged described in the Results; over $c \in [0, 1]$, $\sigma \in [0, 4]$, and $\Theta \in [-1, 3]$ (unimodal inputs), over $s \in [0, 1]$ and $p \in [0, 1]$ (bimodal inputs). In the sidebar, sample distributions with maximal $D_{KL}(P, \tilde{P})$ for $N = 16$; from top, global bimodal inputs, pairwise bimodal inputs, global gaussian inputs, pairwise gaussian inputs.

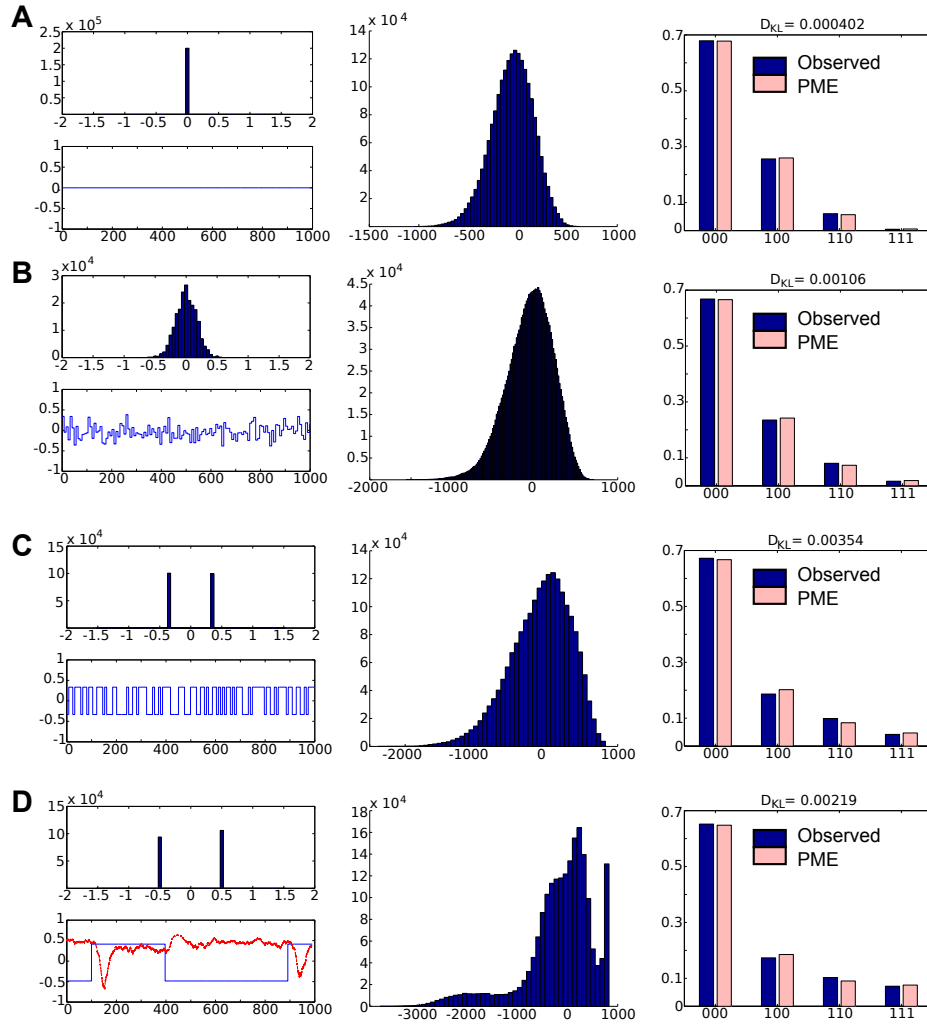


Figure 7: Composite of results for RGC simulations with constant light and full field flicker. In each row, we have (left) a histogram and time series of stimulus, (center) a histogram of excitatory conductances and (right) the resulting distribution on spiking patterns. (A) Gaussian noise only. (B) Gaussian input, standard deviation $1/6$, refresh rate 8 ms. (C) Binary input, standard deviation $1/3$, refresh rate 8 ms. (D) Binary input, standard deviation $1/2$, refresh rate 100 ms. The normalized excitatory conductance (red dashed) is superimposed on the stimulus (blue solid) to illustrate that the LN model that processes light input acts as a (time-shifted) high pass filter.

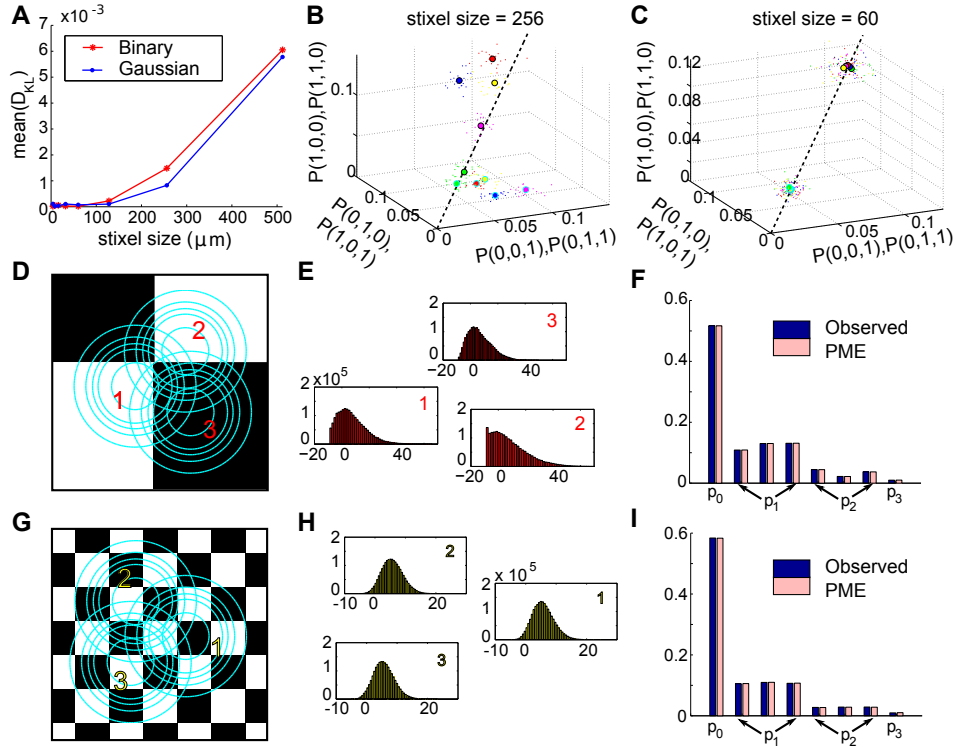


Figure 8: Results for RGC simulations with light stimuli of varying spatial scale (“stixels”). With the exception of (A), we show data from the binary light distributions; results from the Gaussian case are similar. (A) Average $D_{KL}(P, \tilde{P})$ as a function of stixel size. Values were averaged over 5 stimulus positions, each with a different (random) stimulus rotation and translation; $512 \mu\text{m}$ corresponds to full field stimuli. (B,C) Single (black outline) and double (cyan outline) spiking events; individual runs (dots) and averages (large circles). The black line indicates perfect homogeneity among cells (e.g. $P(1, 0, 0) = P(0, 1, 0) = P(0, 0, 1)$). Different colors indicate different stimulus positions. (D-F) Results for one stimulus position, with stixel size $256 \mu\text{m}$. (D) Contour lines of the three receptive fields (at 0.5, 1, 1.5 and 2 SD; and at the zero contour line) superimposed on the stimulus checkerboard (for illustration, pictured in an alternating black/white pattern). (E) Marginal distributions of the excitatory conductances, for each cell. (F) Spike pattern distribution; the three different probabilities labeled p_1 correspond to, e.g. $P(1, 0, 0)$, $P(0, 1, 0)$, and $P(0, 0, 1)$, demonstrating heterogenous responses among the RGCs. (G-I) As in (D-F), but for stixel size $60 \mu\text{m}$.

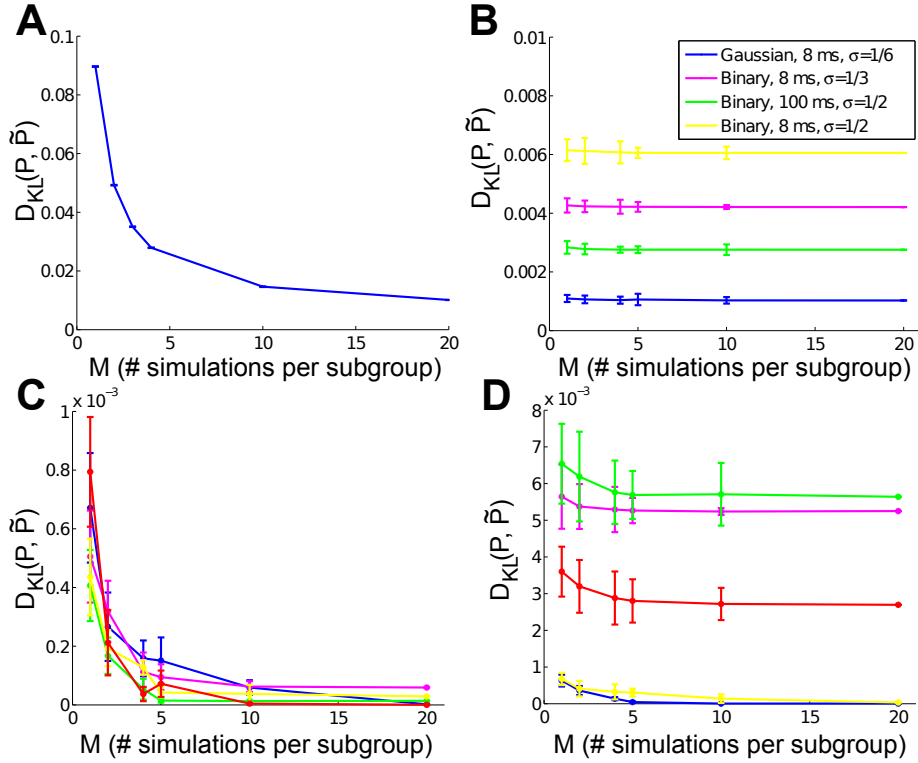


Figure S1: Mean and estimated standard errors of $D_{KL}(P, \tilde{P})$, as a function of subgroup size. The 20 simulations for each circuit condition (see Materials and Methods) were collected into subgroups of $M = 1, 2, 4, 5, 10,$ and 20 . $M = 20$ corresponds to the full simulation length — 2×10^6 ms in (B), 2×10^5 ms in (C,D) — reported in the text. As expected, bias decreases as the length of subgroup increases and asymptotes at — or before — the full simulation length. (A) $N = 16$, Gaussian pairwise inputs, for the sum-and-threshold model. (B) Full-field RGC simulations. (C) Spatially variable RGC simulations, binary stimulus, stixel size = $4 \mu\text{m}$. Different colors signify different positions of stimulus relative to receptive field. (D) As in (C), but stixel size = $256 \mu\text{m}$.